Brushless Doubly-Fed Induction Machines: Torque Ripple

Tim. D. Strous, Xuezhou Wang, Henk Polinder, *Senior Member, IEEE,* and J. A. (Bram) Ferreira, *Fellow, IEEE*

***Abstract*-- The Brushless DFIM without its brush-gear and slip-rings looks promising as successor of the normal DFIG in wind turbine drivetrains. However, the brushless DFIM magnetic field has a rich space-harmonic spectrum, which causes additional torque ripple. This paper focuses on torque ripple in the brushless DFIM. The causes and origin of torque ripple are discussed and an analytical model is developed that derives the torque ripple from the air-gap magnetic field distribution. Further, a FE method for torque ripple calculation is presented. Both methods are used to calculate the torque response of a case study machine. Results are compared and the accuracy of the analytical model is validated with good result. The analytical model is then used to further analyse the torque ripple, resulting in exact torque ripple frequencies and additional insight in the cause of the torque ripple.**

***Index Terms*-- Brushless Doubly-Fed Machine (BDFM), Cross Coupling, DFIG, Space Harmonics, Time Harmonics, Slotting, Torque Ripple.**

I. Introduction

WIND energy is growing rapidly, with a total installed capacity of 336GW halfway 2014, which accumulates to approximately 4% of the total worldwide electricity usage [1]. This rapid growth also increases the need for reliable and fault-tolerant designs, especially for off-shore wind turbines. The Brushless Doubly Fed Induction Machine (DFIM) is an experimental machine type that responds to that concern. This machine type has no brush-gear and slip-rings which increases system reliability and decreases the need for maintenance. Because of this the brushless DFIM is a worthy successor of the normal Doubly Fed Induction Generator (DFIG), which is nowadays the most common machine topology in wind turbines [2].

The brushless DFIM has two stator-windings, the power-winding and the control-winding, with respectively p_p and p_c pole-pairs. A special nested-loop rotor structure ensures coupling with both stator magnetic field components. By connecting the power-winding to the grid and the control-winding to a partially rated Power Electronic (PE) converter, synchronous operation is assured over a limited speed range. Hence, the operating characteristics of the brushless DFIM and the normal DFIG are comparable.

As already indicated in [3] the Brushless DFIM magnetic field distribution has a rich space-harmonic spectrum. This is mainly caused by the nested-loop rotor structure, because the rotor is designed to couple to two main harmonic field components it produces a larger space-harmonic distortion. This affects the machines operating behaviour. The increased rotor space-harmonic distortion increases rotor leakage inductivity, which could be used beneficially to improve voltage ride through performance [4]. The drawback of increased space-harmonics is that it causes additional torque ripple in the machine, which could negatively influence component life-time of the components in a wind turbine drivetrain.

Torque ripple is of great importance for electrical machine (and wind turbine drivetrain) design. Because torque ripple can be expected to be more severe in the brushless DFIM machine type, the main focus of this paper will be on torque ripple modelling and analysis of the brushless DFIM. First, the causes and origin of torque ripple in electrical machines are discussed. Then an analytical model is developed to calculate the torque ripple from the magnetic field distribution of the brushless DFIM. The magnetic field distribution is modelled including the effects of rotor time-harmonics and space-harmonics due to the winding distribution and slotting. The developed model can be used to perform a space- and time-harmonic analysis of the torque ripple in the brushless DFIM. Further, FE techniques for calculating torque ripple are presented in this paper. The developed analytical model is validated with the use of FE calculations, by applying both methods on a case study machine and comparing results. The analytical model is then used to determine the causes and exact frequencies of the different torque ripple components present in the brushless DFIM electromagnetic torque response.

II. Torque Ripple in Electrical Machines

Torque ripple in electrical machines is caused by many factors. By evaluating torque with the use of Fourier theory, it is found that torque ripple can be caused by either space-harmonic components in the air-gap magnetic field or by

The research leading to these results has received funding from the European Union's Seventh Framework Programme managed by REA – Research Executive Agency (FP7/2007_2013) under Grant Agreement N.315485.

T. D. Strous, X. Wang, H. Polinder and J. A. Ferreira are with the Department of Electrical Sustainable Energy, Delft University of Technology, The Netherlands (e-mail: t.d.strous@tudelft.nl)

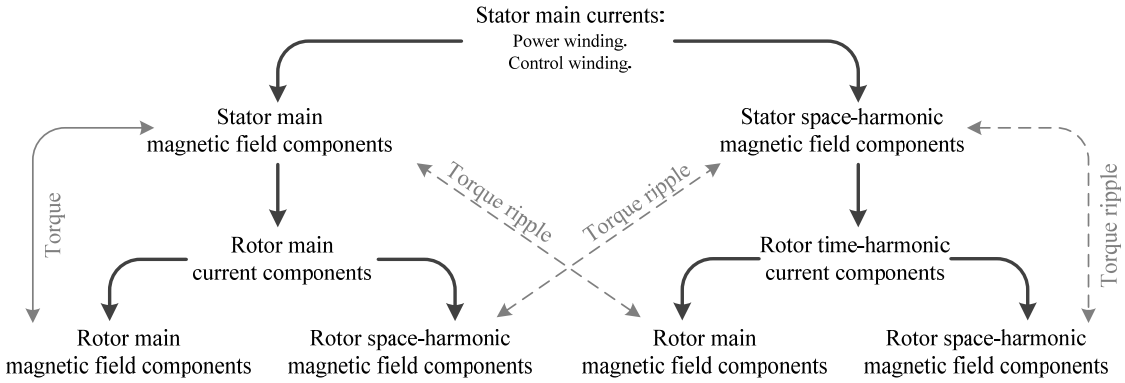

Fig. 1. The effects of space- and time-harmonic components on the torque in a brushless DFIM.

time-harmonic components in the currents flowing through the stator and rotor. The two are related, since space-harmonic magnetic field components, induce time-harmonic components in the currents, which then produce their own set of space-harmonic components in the magnetic field. Although, the latter has smaller influence on the torque, which will be shown in this paper. Torque ripple arises when both stator and rotor produces space-harmonic magnetic field components of the same order, but with different frequencies. The following effects that cause torque ripple can be distinguished:

- Space-harmonic components in the radial air-gap magnetic field distribution, originating from:
  - The winding distribution.
  - Slotting.
  - Saturation:
    Saturation causes the deformation of the magnetic field. (outside the scope of this paper).
  - Mechanical construction:
    Rotor eccentricity or an unbalanced rotor. (outside the scope of this paper)
- Time-harmonic components in the machines currents:
  - Space-harmonic induced time-harmonics.
  - Supplied by the grid or PE converter to the stator-winding currents. (outside the scope of this paper).

The effects causing torque ripple are schematically presented in figure 1. It shows the relations of space- and time-harmonic components and their effect on the torque.

III. Theoretical Development

This section presents the developed models for torque calculations of the brushless DFIM. An analytical torque calculation method is presented, which derives the calculated torque from the linear sheet current density and magnetic field distribution in the air-gap of the brushless DFIM. First an analytical radial air-gap magnetic field distribution model is presented, that includes slotting and winding space-harmonics as well as rotor induced time-harmonics. Then a method for FE torque calculations is presented. Both methods are applied on a case study machine and the results that are obtained are demonstrated. Therefore, first an overview of the case study machine is presented in table I and figure 2.

The model is developed for brushless DFIM's with nested-loop rotor structures, that are operated in synchronous mode of operation. Therefore, the current induced in the rotor nested-loop by the power-winding main magnetic field component, matches the current induced by the control-winding main magnetic field component. Both components have the same frequency and phase-delay between consequent rotor nests [5]. The synchronous rotational speed f_m is then given according:

$$f_m = \frac{f_{pe} - f_{ce}}{N_{nest}} \tag{1}$$

The number of rotor nests N_{nest} must be equal to the number of power-winding p_p and control-winding p_c pole-pairs added.

TABLE I:
Brushless DFIM Design

Construction Parameters			
Number of phases	N_{ph}	3	
Number of pole-pairs	p_p , p_c	4 , 6	
Number of stator slots	N_{ss}	72	
Number of rotor slots	N_{rs}	80	
Number of rotor nests	N_{nest}	10	
Number of loops per nest	q_r	4	
Geometric Parameters			
Axial stack length	l_{stk}	1.6	m
Air-gap length	l_g	1.5	mm
Stator outer radius	r_{so}	0.83	m
Stator inner radius	r_{si}	0.67	m
Rotor outer radius	r_{ro}	0.67	m
Rotor inner radius	r_{ri}	0.58	m
Evaluated operating point			
Power winding frequency	f_{pe}	50	Hz
Control winding frequency	f_{ce}	-10	Hz
Rotational speed	f_m	6	Hz
Power-winding slot current density	J_p	1	A/mm^2
Control-winding slot current density	J_c	1	A/mm^2
Initial position shift	γ_{shift}	(90/N_{nest})	°

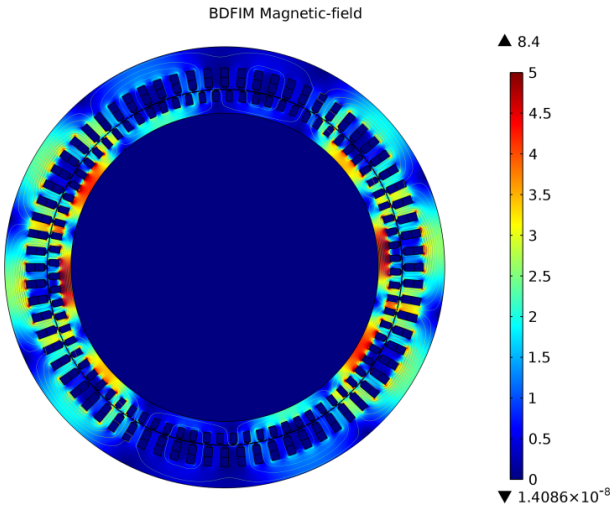

Fig. 2. Case study machine, including 2D magnetic field flux-density.

A. Magnetic Field Modelling

In [6] the radial component of the magnetic flux density distribution B^r_{tot} in the air gap of the brushless DFIM is expressed as the summation of winding space-harmonic components k_s and k_r of respectively the stator B^r_s and rotor B^r_r magnetic fields:

$$B^r_{tot}(\theta^r,t) = B^r_s + B^r_r \tag{2}$$

$$\Rightarrow \quad B^r_s = \Re\left\{\sum_{k_s=-\infty}^{\infty} \underline{B}_{s(k_s)} e^{j(2\pi f_{re(k_s)}t - k_s\theta^r - k_s\gamma_{shift})}\right\}$$

$$\Rightarrow \quad B^r_r = \Re\left\{\sum_{k_s=-\infty}^{\infty}\sum_{k_r=-\infty}^{\infty}\sum_{l=1}^{q_r} \underline{B}_{r,l(k_s,k_r)} e^{j(2\pi f_{re(k_s)}t - k_r\theta^r)}\right\}$$

(2) is expressed in the rotor reference frame as indicated with the superscript *r*. Therefore, the stator magnetic field is found after transformation to the rotor reference frame:

$$\theta^s = \theta^r + \omega_m t + \gamma_{shift} \tag{3}$$

γ_{shift} is a position shift of the rotor with respect to the stator at time $t = 0$. The stator magnetic field consists of the superposition of the power- and control winding field components. Therefore, there are also two main harmonic field components. The p_p^{th} space-harmonic component corresponding to the power-winding and the $-p_c^{th}$ space-harmonic component corresponding to the control-winding. The stator magnetic field components produce time-harmonic rotor currents, each producing its own set of rotor space-harmonic magnetic field components. The set of stator k_s and rotor k_r winding space-harmonics consists of:

$$k_s \in p_p(1-2nN_{ph}) \cup p_c(2nN_{ph}-1) \tag{4}$$

$$k_r \in k_s + nN_{nest} \qquad \forall\ n \in \mathbb{Z} \tag{5}$$

The time-harmonic rotor currents, produced by the stator winding space-harmonic magnetic field components have respective frequencies $f_{re(ks)}$:

$$f_{re(k_s)} = \begin{cases} f_{pe} - k_s f_m & \forall\ k_s \in p_p\left(1-2nN_{ph}\right) \\ f_{ce} - k_s f_m & \forall\ k_s \in p_c\left(2nN_{ph}-1\right) \end{cases} \tag{6}$$

B. Modelling the Magnetic Field including Slotting

The radial air-gap magnetic field distribution of (2) neglects the effect of slotting. This section introduces a slotting function b^r_{slot} to cater for the effect of slotting. Using the slotting function, slotting is then introduced in (2) by a summation of slotting space-harmonic components. The total air-gap magnetic flux density distribution (including slotting effect) $B^r_{tot,slot}$ can then be presented according:

$$B^r_{tot,slot}(\theta^r,t) = \underbrace{B^r_{tot}}_{\text{sum of main+winding harmonics}} + \underbrace{b^r_{slot}B^r_{tot}}_{\text{sum of slotting harmonics}} \tag{7}$$

The slotting function b^r_{slot} consist of a stator $b^r_{s,slot}$ and a rotor $b^r_{r,slot}$ slotting part, which are derived from the air-gap length functions l_{gs} and l_{gr} respectively:

$$b^r_{slot}(\theta^r,t) = \frac{1}{2}\Re\left\{\sum_{k=1}^{\infty}\underline{b}_{s,slot(k_{s,slot})} e^{jk\left(\theta^r+\omega_m t+\gamma_{shift}\right)} + \sum_{k=1}^{\infty}\underline{b}_{r,slot(k_{r,slot})} e^{jk\theta^r}\right\}$$

$$\Rightarrow \quad \frac{1}{2}\frac{l_{g,eff}}{l_{gs}(\theta^s)} \overset{FFT}{\Rightarrow} \sum_{k=0}^{\infty}\underline{b}_{s,slot(k_{s,slot})} \qquad \forall\ k_{s,slot} \in nN_{ss}$$

$$\Rightarrow \quad \frac{1}{2}\frac{l_{g,eff}}{l_{gr}(\theta^r)} \overset{FFT}{\Rightarrow} \sum_{k=0}^{\infty}\underline{b}_{r,slot(k_{r,slot})} \qquad \forall\ k_{r,slot} \in nN_{rs}$$

Here $l_{g,eff}$ is an effective air-gap length, after compensation for the case slotting is not taken into account [7].The air gap length functions express the air-gap length as function of position. Since all equations in this paper are expressed from the rotor reference point of view, the stator air-gap length function changes with position and time. The air-gap length between slots is determined using the straight line circular arc method, as presented in figure 3 [8].

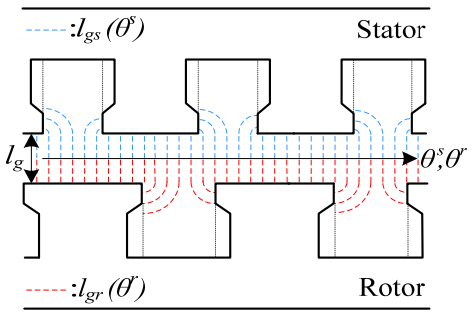

Fig. 3. Air-gap length as function of position angle.

By combining (2),(7) and (8), a distinction can be made between 4 sets of slotting space-harmonics, as is presented in (9):

- Space-harmonic components of order $k_s \pm k_{s,slot}$ due to stator slotting in the stator magnetic field $B^r_{s,slot}$.
- Space-harmonic components of order $k_s \pm k_{r,slot}$ due to rotor slotting in the stator magnetic field $B^r_{s,rslot}$.
- Space-harmonic components of order $k_r \pm k_{s,slot}$ due to stator slotting in the rotor magnetic field $B^r_{r,slot}$.
- Space-harmonic components of order $k_r \pm k_{r,slot}$ due to rotor slotting in the stator magnetic field $B^r_{r,rslot}$.

$$\underbrace{b^r_{slot} B^r_{tot}}_{\text{sum of slotting harmonics}} = B^r_{s,sslot} + B^r_{s,rslot} + B^r_{r,sslot} + B^r_{r,rslot} \tag{9}$$

$$= \underbrace{b^r_{s,slot} B^r_s}_{\{k_s \pm k_{s,slot}\}} + \underbrace{b^r_{r,slot} B^r_s}_{\{k_s \pm k_{r,slot}\}} + \underbrace{b^r_{s,slot} B^r_r}_{\{k_r \pm k_{s,slot}\}} + \underbrace{b^r_{r,slot} B^r_r}_{\{k_r \pm k_{r,slot}\}}$$

Figure 4 presents the modelled stator magnetic field including the effect of stator slotting and the rotor magnetic field including the effect of rotor slotting, modelled for the case study machine described in table I. The effect of rotor slotting in the stator magnetic field and stator slotting in the rotor magnetic field are not shown, for the sake of providing a more clear picture. The total magnetic field distribution is then presented in figure 5. Calculated using the analytical method and validated using FE calculations.

C. *Analytical Torque Calculation Method*

Torque is exerted on the rotor surface S_{rotor} of the brushless DFIM when there is a coupling between stator and rotor magnetic field components of the same space-harmonic order. When these magnetic-field components have a different rotational speed, torque ripple occurs.

A separation can be made between torque due to winding space-harmonics $T_{e,win}$ (including the main torque components) and torque due to slotting harmonics of both stator and rotor, $T_{e,sslot}$ and $T_{e,rslot}$ respectively.

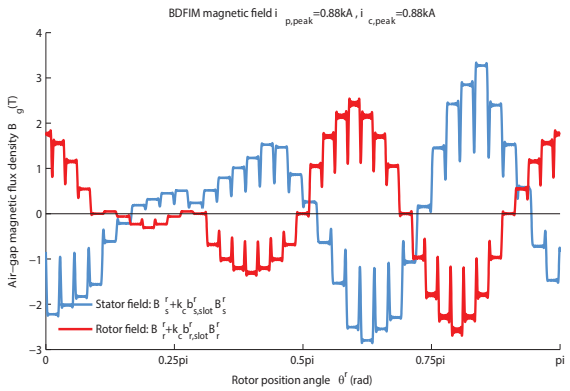

Fig. 4. Brushless DFIM stator and rotor magnetic field components including the effect of slotting

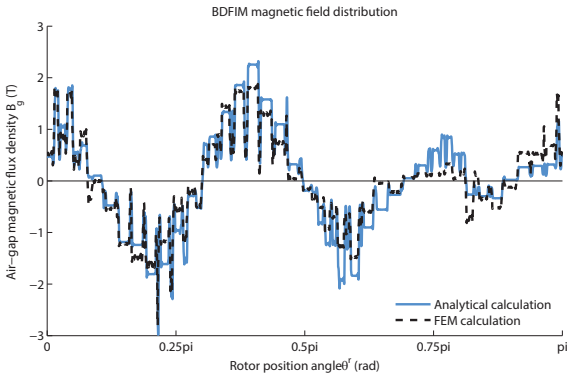

Fig. 5. Brushless DFIM total magnetic field distribution in the air-gap.

[6] already presents an analytical torque calculation method that is derived from the Lorentz-force equation. Using the product of linear sheet current density J^r_r and magnetic field distribution (without slotting), integrated over the rotor surface S_{rotor}, provides the exerted electro-magnetic torque $T_{e,win}$.

$$T_{e,win}(t) = r_{ro} \iint J^r_r \, B^r_{tot} \, dS_{rotor} \tag{10}$$

$$= l_{stk} \, r_{ro}^2 \sum_{k_{time}} \sum_{k_{space}} \int_{\theta^r=0}^{2\pi} J^r_{r(k_{time},k_{space})} \, B^r_{s(k_{space})} \, d\theta^r$$

$$\Rightarrow k_{space} \in k_r \cap \pm k_s$$

$$\Rightarrow k_{time} \in \{k_s, k_s \pm k_{s,slot}\}$$

The linear sheet current density distribution can be derived from the magnetic field distribution according:

$$J^r_r(\theta^r, t) = \frac{l_{g,eff}}{\mu_0} \frac{1}{r_{ro}} \frac{\partial B^r_r}{\partial \theta^r} \tag{11}$$

Here μ_0 is the magnetic permeability of air ($4\pi \cdot 10^{-7}$ H/m). (10) includes the brushless DFIM main torque components as well as the torque ripple components due to winding space-harmonics and space-harmonic induced rotor time-harmonics. The torque ripple frequencies f_T produced by the magnetic field components of space-harmonic order k_{space}, are given by:

$$f_{T(k_{space},k_{time})} = f_{re(k_{time})} \pm f_{re(k_{space})} \tag{12}$$

Table II provides an overview of winding space-harmonic components causing torque ripple, calculated according (10), for the case study machine presented in table I. Also the corresponding torque ripple frequencies f_T are presented, as calculated in (12).

TABLE II:
Winding torque ripple components and frequencies

Main time-harmonics:	$f_{re(4)}=f_{re(-6)}$ = 26 Hz							
k_{space}	**4**	**-6**	44	-66	-76	114	-116	124
f_T **(Hz)**	**0**	**0**	340	380	380	700	720	720
Rotor time-harmonic:	$f_{re(-20)}$ = 170 Hz							
k_{space}	-	-	-	-	-	-	-	-
f_T **(Hz)**	-	-	-	-	-	-	-	-
Rotor time-harmonic:	$f_{re(-28)}$ = 118 Hz							
k_{space}	28	-42	-52	68	78	-92	-102	138
f_T **(Hz)**	0	360	380	340	340	720	740	720
Rotor time-harmonic:	$f_{re(30)}$ = 190 Hz							
k_{space}	-	-	-	-	-	-	-	-
f_T **(Hz)**	-	-	-	-	-	-	-	-
Rotor time-harmonic:	$f_{re(-42)}$ = 242 Hz							
k_{space}	28	-42	-52	68	78	-92	-102	138
f_T **(Hz)**	360	0	20	700	700	360	360	1080

Using the same methodology, the torque ripple due to stator and rotor slotting harmonics can be taken into account. However, the Lorentz-force equation in (10) uses the magnetic field of the stator and the linear sheet current density of the rotor for calculating the torque. The linear sheet current density obviously does not take into account the effect of slotting. Therefore, first the torque ripple $T_{e,sslot}$ due to the interaction of stator magnetic field slotting space-harmonics of order $k_s \pm k_{s,slot}$ coupling with the rotor magnetic field winding space-harmonics is taken into account:

$$\begin{aligned} T_{e,sslot}(t) &= r_{ro}\iint\left(J_r^r\, B_{s,sslot}^r\right)dS_{rotor} \\ &= l_{stk} r_{ro}{}^2 \sum_{k_{time}}\sum_{k_{space}}\int_{\theta^r=0}^{2\pi} J_{r(k_{time},k_{space})}^r B_{s,sslot(k_{space})}^r d\theta^r \\ \Rightarrow k_{space} &\in k_r \cap \pm\left(k_s \pm k_{s,slot}\right) \\ \Rightarrow k_{time} &\in \left\{k_s, k_s \pm k_{s,slot}\right\} \end{aligned} \tag{13}$$

Then the torque ripple $T_{e,rslot}$ due to the interaction of rotor magnetic field slotting space-harmonics of order $k_r \pm k_{r,slot}$ with the stator magnetic field winding space-harmonics is provided:

$$\begin{aligned} T_{e,rslot}(t) &= -r_{si}\iint\left(J_s^r\, B_{r,rslot}^r\right)dS_{rotor} \\ &= -l_{stk} r_{ro} r_{si} \sum_{k_{time}}\sum_{k_{space}}\int_{\theta^r=0}^{2\pi} J_{s(k_{space})}^r B_{r,rslot(k_{time},k_{space})}^r d\theta^r \\ \Rightarrow k_{space} &\in k_s \cap \pm\left(k_r \pm k_{r,slot}\right) \\ \Rightarrow k_{time} &\in \left\{k_s, k_s \pm k_{s,slot}\right\} \end{aligned} \tag{14}$$

The negative sign in (14) is due to the calculation of torque exerted on the stator, which has an opposite sign from the torque exerted on the rotor. Table III provides an overview of stator and rotor slotting space-harmonic components causing torque ripple and the corresponding torque ripple frequencies for the case study machine presented in table I.

TABLE III:
Slotting torque ripple components and frequencies

Stator slotting:	$f_{re(4)}=f_{re(-6)}$ = 26 Hz (Main time-harmonic)					
k_{space}	76	66	-44	-114	-76	-164
$k_s \pm k_{s,slot}$	4+72	-6+72	28-72	-42-72	-20+144	-20-144
f_T **(Hz)**	380	380	340	700	720	1060
Rotor slotting:	$f_{re(4)}=f_{re(-6)}$ = 26 Hz (Main time-harmonic)					
k_{space}	-76	-66	114	44	164	174
$k_r \pm k_{r,slot}$	4-80	14-80	34+80	-36+80	4+160	14+160
f_T **(Hz)**	380	380	700	340	1060	1080

D. FE Torque Calculation Method

The electro-magnetic torque in the machine can be derived from the magnetic field in the air-gap of the brushless DFIM. Applying Maxwell's stress tensor method, a circular integral of the 2-dimensional magnetic field around the air-gap circumference at radius r_g is calculated to obtain the electromagnetic torque T_e:

$$T_e = \frac{l_{stk}}{\mu_0} r_g^2 \int_0^{2\pi} B_r B_{\tan} d\theta \tag{15}$$

Here B_r and B_{tan} are the radial and tangential components of the flux density in the air-gap at radius r_g. Equation (15) can easily be applied on a FE derived magnetic field as presented in figure 2. However a 2D FE program solves the magnetic vector potential A_z (in axial z-direction). The flux density distribution $\boldsymbol{B}$ is derived from A_z according (16) and hence one order less accurate.

$$B_r = \frac{\partial A_z}{r_g \partial\theta}; \qquad B_{\tan} = -\frac{\partial A_z}{\partial r_g} \tag{16}$$

To improve the calculations accuracy, an analytical filter is applied to Maxwell's stress tensor method. As is described in [9]. This method reduces the sensitivity to FE meshing parameters. First the flux density B is derived from an analytical expression of A_z in a shell in the air-gap. This air-gap shell is defined by two concentric circles in the air-gap with respective radii r_1 and r_2, where ($r_1 < r_g < r_2$). At the boundaries of this air-gap shell A_z can analytically be expressed as a Fourier series of space-harmonic components k:

$$\begin{aligned} A_z(r_1,\theta) &= a_{01} + \sum_{k=1}^{\infty}\left[a_{k1}\cos(k\theta) + b_{k1}\sin(k\theta)\right] \\ A_z(r_2,\theta) &= a_{02} + \sum_{k=1}^{\infty}\left[a_{k2}\cos(k\theta) + b_{k2}\sin(k\theta)\right] \end{aligned} \tag{17}$$

From (15)-(17) the improved computational equation for deriving the electro-magnetic torque is derived:

$$T_e = 2\pi\frac{l_{stk}}{\mu_0}\sum_{k=1}^{\infty}\frac{k^2}{\left(\frac{r_1}{r_2}\right)^k - \left(\frac{r_2}{r_1}\right)^k}\left(a_{k2}b_{k1} - a_{k1}b_{k2}\right) \tag{18}$$

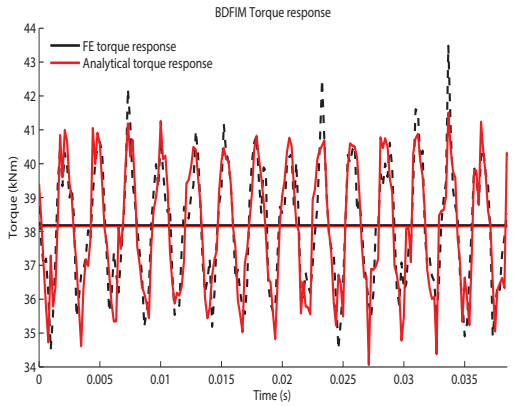

Fig. 6. Brushless DFIM torque response during nominal operation.

IV. Torque Evaluation

Sections III-C and -D presented methods for calculating torque and torque ripple in a brushless DFIM using analytical calculations and FE calculations respectively. Both methods are applied on the brushless DFIM design as presented in Table I. The generated torque responses for a calculation time of one rotor electric period ($1/f_{re} = 38.5ms$) are presented in figure 6. The analytical calculation method is validated by the FE calculation method. The resulting analytical calculated torque response has a good accuracy, when compared to the FE calculated torque response.

With the use of (19) the torque ripple is expressed as a percentage of the mean torque. This provides a good measure for the torque ripple in this machine at its nominal operating point.

$$T_{ripple} = \frac{T_{e,\max} - T_{e,\min}}{T_{e,mean}} \cdot 100\% \qquad (19)$$

The resulting mean torque T_{mean} and torque ripple T_{ripple} for both the analytical and the FE calculation method are compared in Table IV.

The advantage of the analytical model over a FE model is that it helps identifying the cause of the torque ripple and additionally to determine the exact torque ripple frequencies. Figures 7 until 9 provide an evaluation of torque ripple amplitudes due to different space-harmonic components and their corresponding frequencies. Figure 7 first presents the torque components due to winding space-harmonics only. Following (10) and (12). Since the main torque is caused by the main winding space-harmonic components (e.g. the 4th and the -6th), these are also indicated in figure 7 (By the uncompleted grey bars). Figure 8 then presents the torque ripple components and their corresponding frequencies due to time-harmonics in the rotor magnetic field. (e.g. all rotor magnetic field components not generated by the main rotor current $k_{time} \notin \{4,-6\}$). Last, figure 9 presents all torque components and their corresponding frequencies due to slotting harmonics, including stator and rotor slotting as well as torque components due to time-harmonics induced by the stator slotting space-harmonics, according (12)-(14).

TABLE IV:
Torque ripple calculation method comparison

	T_{mean}:	T_{ripple}:
Analytical calculation:	38.1kNm	20%
FE calculation:	38.2kNm	23%

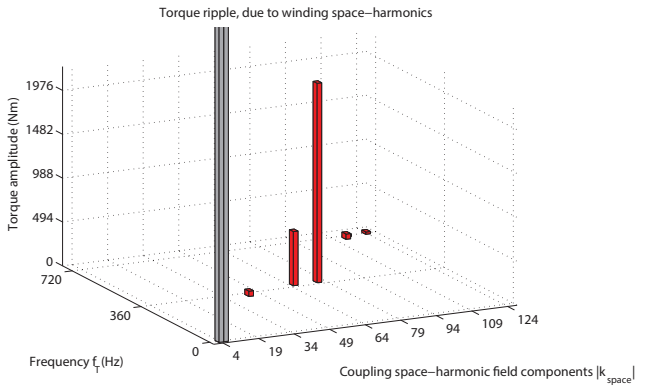

Fig. 7. Torque ripple components due to the winding distribution space-harmonics, without taking into account time-harmonics.

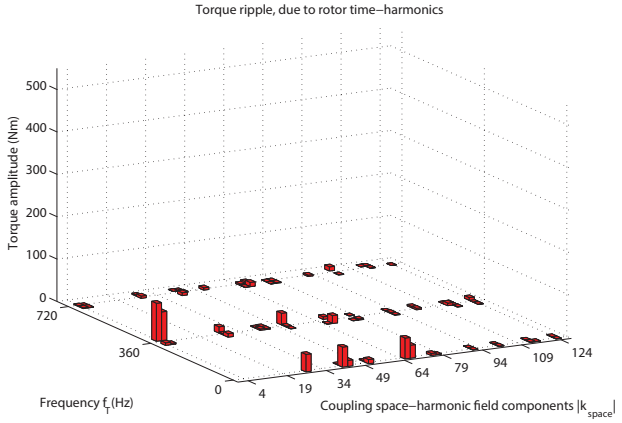

Fig. 8. Torque ripple components due to rotor time- harmonic induced field components

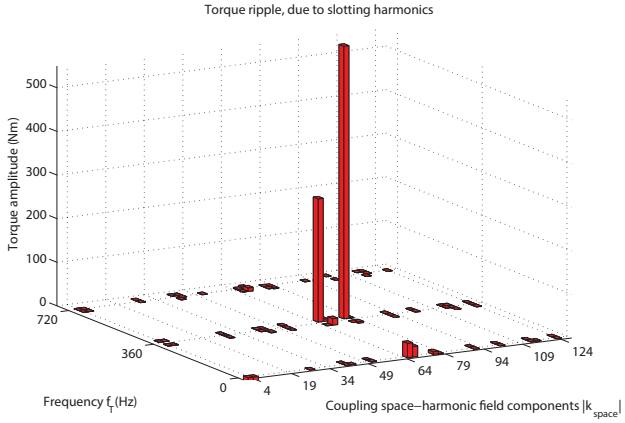

Fig. 9. Torque ripple due to slotting harmonics and slotting harmonic induced rotor time-harmonics.

From figures 7 until 9 can be concluded that for the case study machine as presented in table I, the largest contribution to the torque ripple is caused by winding space-harmonics. Slotting space-harmonics also contribute to the torque ripple, but to a lesser extent. The effect of the rotor time-harmonics, induced by the stator space-harmonics, on the torque ripple is negligible. Interesting is to see that the rotor time-harmonics also produce torque components at 0 Hz. These are the torque components responsible for the crawling effect in normal induction machines.

The 66^{th} and 76^{th} space-harmonic field components have the largest contribution to the torque ripple. Both these space harmonic field components produce a ripple frequency of 380Hz at the specified operating point. The power- and the control-winding distribution as well as stator and rotor slotting harmonics all contribute to the 66^{th} and 76^{th} space-harmonic components, as can be seen from table's II and III. This explains why they contribute most to the torque ripple.

V. Conclusion

This paper first discussed the causes of torque ripple in electrical machines and explained their origin due to space-harmonic components in the air-gap magnetic field or time-harmonic components in the currents flowing through the machines windings.

Two methods for torque calculations were introduced. An analytical method and a FE method. The analytical method derives the torque from the radial air-gap magnetic field distribution using the Lorentz-force equation. The air-gap magnetic field is modelled including the effects of winding space-harmonics, slotting and rotor time-harmonics. The FE torque calculation on the other hand is based on Maxwell's stress tensor method, where an analytical filter is applied for improved accuracy.

With the use of a case study machine, the analytical torque calculation method is validated by comparison to the FE torque calculation method. The analytical derived mean torque and torque ripple where calculated with good accuracy.

With the use of the analytical torque calculation method it is further possible to determine the space- and time-harmonic components contributing most to the torque ripple and to determine their origin. Their corresponding ripple frequencies can also be derived. When analyzing the case study machine it was found that the largest contribution to the torque ripple was caused by the winding distribution space-harmonics. This verifies that the excessive space-harmonic spectrum, present in the nested-loop rotor structure of the brushless DFIM, also has an considerable effect on the torque ripple. The effect of time-harmonic rotor currents was found to be negligible. The effect of slotting (half open stator and rotor slots) in the case study machine also has some contribution to the torque ripple.

VI. References

[1] WWEA half-year report 2014 [Online]. Available: http://www.wwindea.org/webimages/WWEA_half_year_report_2014.pdf

[2] R. A. McMahon, X. Wan, E. Abdi-Jalebi, P. Tavner, P. C. Roberts, and M. Jagiela, "The BDFM as a generator in wind turbines," in *12th Int. Power Electron. Motion Control Conf.,* EPE-PEMC, 2006, pp. 1859–1865.

[3] H. Goringpour, B. Jandaghi, H. Oraee,"Time and Space Harmonics in Brushless Doubly-Fed Machine," in *19th Iranian Conf. Elect. Eng. (ICEE),* 2011, pp. 1–6.

[4] U. Shipurkar, T. D. Strous, H. Polinder, and J. A. Ferreira, "LVRT performance of brushless doubly-fed induction machines - a comparison," to be presented at *Int. Conf. Elect. Machines & Drives (IEMDC),* 2015.

[5] S. Williamson, A. C. Ferreira, A. K. Wallace, "Generalised theory of the brushless doubly fed machine. Part I : Analysis," in *IEE Proc.-Elect. Power Appl*., vol. 144, no. 2, 1997, pp. 111-122.

[6] T. D. Strous, N. H. van der Blij, H. Polinder, and J. A. Ferreira, "Brushless doubly-fed induction machines: Magnetic field modelling," in *Int. Conf. Elect. Machines (ICEM),* Sep. 2014, pp. 2702–2708.

[7] J. Pyrhönen, T. Jokinen, V. Hrabovcová, *Design of Rotating Electrical Machines,* 1st ed., John Wiley & Sons, 2008.

[8] D. C. Hanselman, *Brushless permanent-magnet motor design,* McGraw-Hill, 1994.

[9] M. Popescu, D.M. Ionel, T.J.E. Miller, S.J. Dellinger and M.I. McGilp, "Improved finite element computations of torque in brushless permanent magnet motors," in *IEE Proc.-Elect. Power Appl.*, vol. 152, no. 2, 2005, pp. 271-276.